Induced capillary dipoles in floating particle assemblies

M. Delens ⓘ, Y. Collard ⓘ, and N. Vandewalle ⓘ
GRASP, Physics Department, University de Liège, Belgium

Capillary-driven self-assembly is a common fabrication method that consists of placing floating particles onto a liquid-air interface. The attractive interaction between particles is due to the local deformations of the interface and is often described via so-called capillary charges. This approach holds for similar particles far from each other. When particles are close together or when they differ in size, their contact lines become tilted. By using different spherical particles, we show evidence experimentally that the capillary interaction becomes far more complex. We propose to consider induced capillary dipoles to model the menisci, therefore providing an extra attraction at short distances. This effect is enhanced for particles of different sizes such that binary self-assemblies reveal unusual local ordering.

In the last two decades, capillary-driven self-assembly has been proposed as a promising fabrication method at the mesoscopic scale, i.e., in between usual bottom-up and top-down fabrication methods [1–3]. Capillary-driven self-assembly consists of gently placing floating particles at some liquid-air interface. Local deformation of the liquid interface appears around each particle depending on the particle's shape, buoyancy, and wetting properties [4–6]. These deformations of the interface can cause particles to aggregate and eventually form patterns. A popular approach describes the interaction by considering so-called capillary charges to characterize the local deformation around each particle. Capillary charges can be encoded on the particles using surface treatment [7], or by designing specific particle shapes [6], opening ways to self-assemble elaborated structures. Using these properties, self-assembly has been exploited to achieve an impressive number of complex tasks in microfluidic, including low-Reynolds-number mixing [8,9], microfabrication [10,11], drug delivery [12], cargo transport [13], sensing [14], or photonics [15,16]. However, the accurate measurement of the capillary force between the components, driving the dynamics, is a complex problem and has been done recently in independent works [17,18]. It has been shown [18] that the capillary charge representation fails to capture the interaction when particles come close together, or when particles have quite different sizes or depths. The present work aims to collect accurate data and to provide an elegant way to model those situations.

Our experimental setup, sketched in Fig. 1, is as following. Spherical beads of alloy AISI 52 100, a soft ferromagnetic alloy, are deposited on an air-water interface where they float thanks to the surface tension. The density ρ_s of the particles is 7800 kg/m^3. Three diameter sizes are used: $d = 400$ μm, 500 μm, and 800 μm. Due to their high volumic mass, the beads are more than 90% submerged such that the radius of the contact line $a \approx d/4$. More precisely, we have measured the contact line radius to be approximately 80 μm, 180 μm, and 230 μm for the respective particle diameters of 400 μm, 500 μm, and 800 μm. A picture of an 800 μm bead and its contact line is shown in Fig. 2. The particles have an apparent magnetic susceptibility χ close to three. The water bath is surrounded by one pair of Helmholtz coils creating a spatially uniform vertical magnetic field B_z, inducing vertical magnetic moments inside the particles. In that case, the bead attraction can be counterbalanced by magnetic dipole-dipole repulsion. This repulsion can be precisely tuned by the
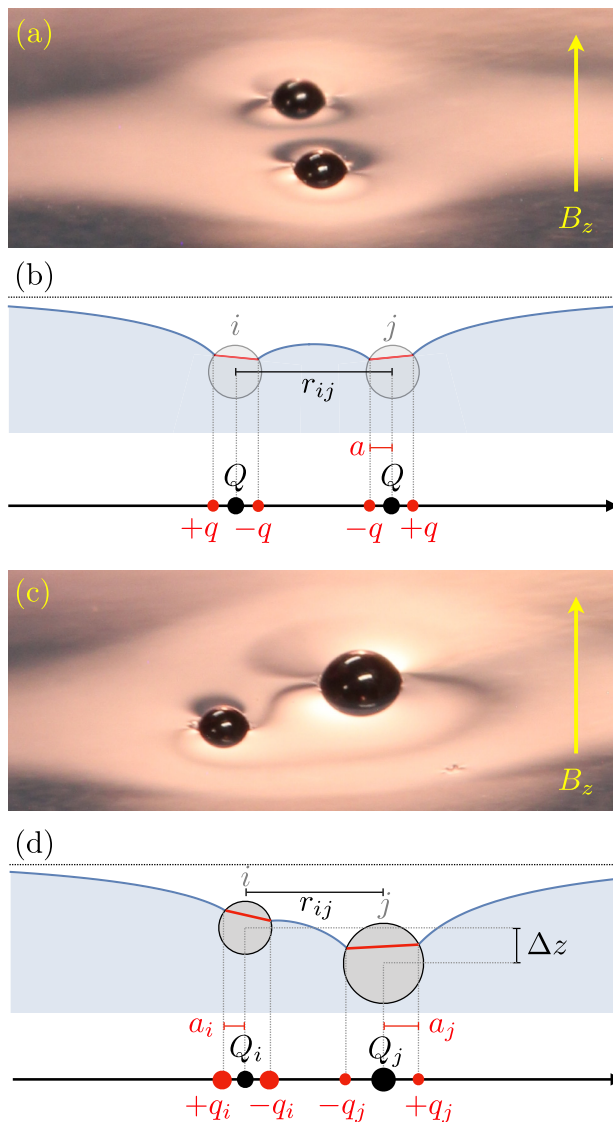
FIG. 1. (a) Picture of two $400\,\mu$m soft ferromagnetic beads floating on the water-air interface under a vertical magnetic field B_z. (b) Sketch of the equilibrium situation for two identical beads. The contact line, denoted in red, is pinned and has a radius a. Each particle is described by a capillary charge Q and dipolar components $\pm q$. (c) Picture of a $400\,\mu$m and an $800\,\mu$m bead at equilibrium. (d) Equilibrium distance r_{ij} between nonequivalent spheres involves a depth difference Δz but also locally steeper slopes. Each particle i is described by a central charge Q_i and dipolar components $\pm q_i$ at a distance a_i from its center.

magnetic field, thanks to the soft ferromagnetic properties exhibited by the particles. When the field B_z is larger than a threshold, typically of a few dozen of Gauss, the magnetocapillary binding leads to an equilibrium distance $r^\star$ larger than the bead diameters, avoiding contact [19,20]. Figure 1 shows pictures of equilibrium situations for identical particles (a) and an asymmetric pair (c). Measuring the equilibrium distance provides an elegant way to evaluate the capillary attraction between floating spheres with high precision, as will be presented below.
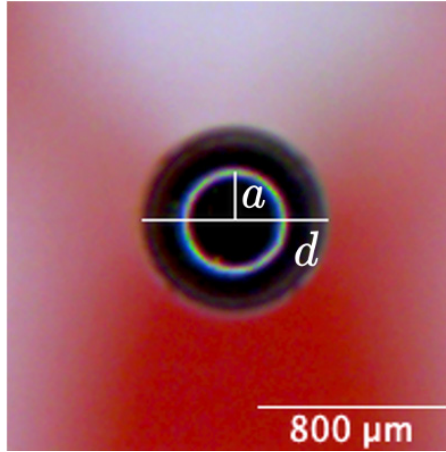
FIG. 2. Top view of an 800 μm bead floating on a water-air interface. A ring light highlights the contact line, enabling accurate measurements. The bead diameter d and contact line radius a are depicted in white.

Considering a spherical floating particle, it has been shown that the elevation of the interface z, at a distance r from a particle center, has the analytical form

$$z(r) = Q K_0\left(\frac{r}{\lambda}\right), \tag{1}$$

where K_0 is a modified Bessel function of the second kind and order zero [21–23]. The typical distance over which the liquid surface is deformed is called the capillary length $\lambda = \sqrt{\gamma/\rho g}$ and $\lambda = 2.7$ mm for water. The characteristic deviation length Q, usually called capillary charge in the literature, depends on various physical properties like the size of the particle, the surface tension γ, the liquid density ρ, or the wetting properties of the particle [21–23]. Capillary charge Q will be positive for a convex meniscus and negative for a concave meniscus. With the meniscus around our particles being concave, it is therefore represented by a negative capillary charge Q in this article. As calculated by Vella and others, for a spherical bead of density $\rho_s > \rho_w$, Q is proportional to the particle volume V and is given by

$$Q = \frac{R^3}{\lambda^2}\left(\frac{2\rho_s/\rho_w - 1}{3} - \frac{\cos(\theta)}{2} + \frac{\cos(\theta)^3}{6}\right), \tag{2}$$

where θ is the contact angle and we have measured $\theta \approx 75°$ for our beads [21]. Capillary charges of our particles can therefore be calculated using Eq. (2). We find -5 μm, -10 μm, and -42 μm for the respective particle diameters 400 μm, 500 μm, and 800 μm.

When two particles i and j are placed on the interface with a separating distance r_{ij}, each particle feels the deformation created by the other one. Assuming that the superposition principle holds for surface deformations [26], the particles interact according to the capillary interaction potential given by

$$U_{QQ} = -2\pi\gamma Q_i Q_j K_0\left(\frac{r_{ij}}{\lambda}\right) \tag{3}$$

[4,23,24]. Particles with similar wetting properties will therefore attract each other and form floating aggregates [25]. This phenomenon is colloquially called the Cheerios effect, referring to the cereals aggregating in a milk bowl [21]. This approach using monopolar capillary charge has been extensively used in the case of spherical particles. However, when particles are coming close together, the superposition principle does not hold anymore [26]. This can be understood in the sketch of Figs. 1(b) and 1(d). The contact lines pinned on the particles, which are horizontal when

far from each other, start to tilt more and more when particles come closer [27]. This effect is more present for asymmetric cases, i.e., when different particle sizes are used, as sketched in Fig. 1(d). Please note that the contact lines can only tilt when they are pinned on the spherical particles. Indeed, if the contact angle is fixed, the spheres would rotate to keep a horizontal contact line until they are very close and where the contact line would undulate [28]. Inclined pinned contact lines have been numerically studied by Cooray *et al.* [29] only for identical spheres. They calculated up to 30% extra attraction when beads come close together. Another nice experiment using magnetic disks resting at a fluid interface has demonstrated a spontaneous tilting of the disks at short distances and extra attraction has also been measured [17]. Many anisotropic objects such as cylinders, tilted magnetic ellipsoids, as well as planar particles with hydrophilic and hydrophobic faces tilt on fluid-fluid interfaces and thus also present a tilted contact line [30–34]. Analytical models or experiments to study the tilt of the contact line between two spheres are still lacking.

The magnetocapillary interaction potential between two soft-ferromagnetic beads i and j separated by a distance r_{ij} is therefore given by

$$U_{\mathrm{Mc}} = -2\pi\gamma Q_i Q_j K_0\left(\frac{r_{ij}}{\lambda}\right) + \frac{\mu_0}{4\pi}\frac{\mu_i\mu_j}{r_{ij}^3}, \tag{4}$$

where one recognizes the capillary attraction U_{QQ} in the first term of the right hand. The second term is the magnetic repulsion U_M induced by a vertical magnetic field B_z. The magnetic moment μ_i is directly proportional to the field strength B_z and to the volume V_i of particle i. As a consequence, both terms in Eq. (4) are proportional to the product of particle volumes. The interaction potential can be rewritten in dimensionless units such that

$$u_{\mathrm{Mc}} = -K_0(x_{ij}) + \frac{\mathrm{Mc}}{x_{ij}^3}, \tag{5}$$

where x_{ij} is the distance r_{ij} normalized by the capillary length and

$$\mathrm{Mc} = \kappa B_z^2 = \frac{\chi^2 V_i V_j}{8\pi^2\mu_0\gamma Q_i Q_j\lambda^3}B_z^2 = \frac{2\chi^2\lambda}{9\gamma\mu_0\left(\frac{2\rho_s/\rho_w-1}{3} - \frac{\cos(\theta)}{2} + \frac{\cos(\theta)^3}{6}\right)^2}B_z^2 \tag{6}$$

is the magnetocapillary number capturing the competition between capillary and magnetic effects and already defined in other studies [20,35–38]. The factor κ is independent of particle sizes, meaning that the interaction potential is also independent. For $\theta = 75°$, we found $\kappa = 2.62\,10^{-5}\,\mathrm{G}^{-2}$. The potential u_{Mc} has a minimum corresponding to the equilibrium distance $r^\star = \lambda x^\star$. The only control parameter remaining in Eq.(5) is the field strength B_z via Mc. This nice property allows us to build many different floating crystals varying the lattice spacing [19,20,39].

We first realized series of accurate measurements for the equilibrium distance $r^\star$ between two particles where different particle diameters are considered; $d_i = \{400, 500, 800\}\,\mu\mathrm{m}$. In Fig. 3, the resulting center-to-center distances $r^\star$ as a function of B_z are drawn for all pairs of particles. Horizontal dashed lines are drawn to define the center-to-center distance at which the beads come into contact. In all cases, the equilibrium distances show a monotonic behavior as a function of B_z. However, the data do not overlap on a single black curve as expected with the dimensionless potential u_{Mc} described in Eq. (5).

Considering symmetrical cases, one observes an increase of the capillary attraction, i.e., a slight decrease of $r^\star$, when d grows. For asymmetrical cases, the deviation from the model presented in Eq. (5) is even more pronounced. In both cases (symmetric and asymmetric), the experimental equilibrium distance $r^\star$ is always smaller than the one predicted by the model.

In order to tackle the complex dispersion of data points reported above, one should identify the different origins of the deviation of the equilibrium distance $r^\star$ from the model presented in Eq. (5). In fact, two physical effects are taking place: (i) an additional capillary effect due to tilted contact lines as sketched in Figs. 1(b) and 1(d), increasing the capillary attraction; and (ii) a small reduction of magnetic repulsion only in asymmetric systems due to a difference Δz of particle depths as
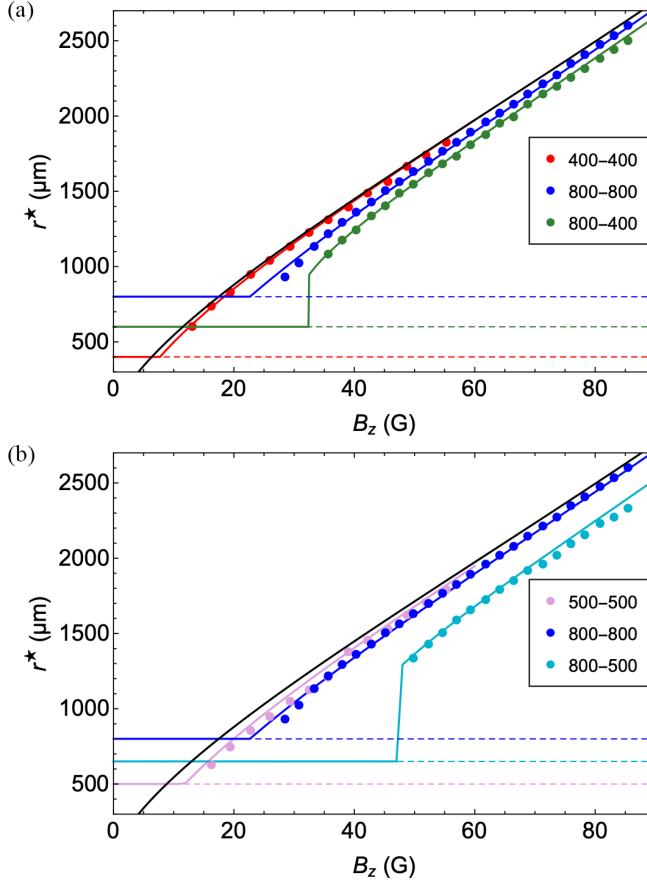
FIG. 3. Experimental data of equilibrium distances $r^\star$ as a function of B_z for (a): pairs of $d = 400$ μm, and $d = 800$ μm, and the asymmetrical case $d_1 = 400$ μm and $d_2 = 800$ μm and (b): pairs of $d = 500$ μm and $d = 800$ μm, and the asymmetrical case $d_1 = 500$ μm and $d_2 = 800$ μm. In most cases, the error bars are smaller than the symbol size. At low field values, near the particle contact, the error bars are three times the symbol size. The black upper curve is the equilibrium distance of the potential u_{Mc} described in Eq. (5). Colored curves are equilibrium distances predicted by our model u_{Mc+} described in Eq. (10).

sketched in Fig. 1(d). The increase in attraction between the beads combined with the reduction in magnetic repulsion between them explains why the experimental values of $r^\star$ are lower than those predicted by the model.

Let us consider the following observation: when two particles come together, the contact line of diameter $2a$ around each particle becomes tilted. This inclination of the contact line may induce extra attraction between particles. In order to model this effect, we propose to add a positive and a negative charge $\pm q$ around each particle, as shown in Figs. 1(b) and 1(d). Therefore, the total capillary charge Q of each particle remains unchanged but a capillary dipole of size $2a$ has been added. More precisely, the dipolar charges $\pm q_j$ induced on particle j come from the slope $\frac{\partial z}{\partial r}$ generated by the presence of the particle i. Taking the derivative of Eq. (1), this induced charge is given by

$$q_j = \frac{a_j Q_i}{\lambda} K_1\left(\frac{r_{ij}}{\lambda}\right). \tag{7}$$

Those additional charges $\pm q_j$ should be placed in the line joining the two-particle centers at distance $r_{ij} \pm a$ from particle i. A similar capillary dipole will appear on particle i as induced by the presence

of particle j. In order to evaluate the total interaction potential between particles i and j, one has to consider the interactions between all the capillary charges of particle i $\{Q_i, +q_i, -q_i\}$ and particle j $\{Q_j, +q_j, -q_j\}$. As a first approximation, the resulting capillary interaction potential between two spheres should include the capillary potential U_{QQ}, presented in Eq. (3), plus a charge-dipole U_{Qd} potential. The capillary charge-dipole interaction U_{Qd} considers the interaction between a charge Q and the induced dipolar charges $\pm q$ of the opposite particle. Each case has attractive and repulsive components like

$$U_{Qd} = -2\pi\gamma Q_i q_j K_0\left(\frac{r_{ij}-a_j}{\lambda}\right) + 2\pi\gamma Q_i q_j K_0\left(\frac{r_{ij}+a_j}{\lambda}\right) - 2\pi\gamma Q_j q_i K_0\left(\frac{r_{ij}-a_i}{\lambda}\right)$$
$$+ 2\pi\gamma Q_j q_i K_0\left(\frac{r_{ij}+a_i}{\lambda}\right). \tag{8}$$

Taking into account Eq. (7), and by developing the Bessel functions K_0 around r with $a \ll r$, one obtains the leading terms,

$$U_{Qd} = -4\pi\gamma\left[Q_i^2\frac{a_j^2}{\lambda^2} + Q_j^2\frac{a_i^2}{\lambda^2}\right]K_1^2\left(\frac{r_{ij}}{\lambda}\right), \tag{9}$$

which is always attractive. Using the same process, we determine that the interaction between the capillary dipoles, denoted as U_{dd}, scales as $(1/r)K_1^3(r/\lambda)$. However, this interaction term becomes negligible compared to U_{QQ} and U_{Qd} when $r < \lambda$. Consequently, U_{dd} and the subsequent terms of the multipolar expansion are not significant and can be disregarded. Hence, the total capillary interaction potential is given by $U_{QQ} + U_{Qd}$, which can be made dimensionless by dividing by the factor $2\pi\gamma Q_i Q_j$ representing the characteristic capillary energy in the system. Finally, the dimensionless magnetocapillary interaction potential of Eq. (5) becomes

$$u_{Mc^+} = -\left[K_0(x_{ij}) + 2\left(\frac{Q_i^2 a_j^2 + Q_j^2 a_i^2}{\lambda^2 Q_i Q_j}\right)K_1^2(x_{ij})\right] + \frac{Mc}{x_{ij}^3}\left[1 - 3\left(\frac{\Delta z}{\lambda x_{ij}}\right)^2\right], \tag{10}$$

where only leading terms are considered. The capillary attraction, given in the first large brackets, is seen to be modified since the K_1^2 term has significant value with respect to K_0 when $r < \lambda$. When the ratio between contact line radii a and capillary length λ tends to zero, one recovers the capillary attraction of the previous model. Please note that the factor $(Q_i^2 a_j^2 + Q_j^2 a_i^2)/\lambda^2 Q_i Q_j$ in the charge-dipole term is highly nonlinear and increases rapidly with the asymmetry of the system. Moreover, in asymmetrical cases only, the depth difference Δz of the particle centers impacts the magnetic repulsion. Indeed, the magnetic potential, given by the last term of Eq. (10), is reduced by a simple factor $[1 - 3(\Delta z/\lambda x_{ij})^2]$. In the symmetrical cases, the depth difference equals zero, and one recovers the dimensionless magnetic potential described by the second term in Eq. (5).

In Fig. 3, the equilibrium distances predicted by our induced dipoles model u_{Mc^+} are plotted for beads with identical diameters (red, violet, and blue curves). We observe that the theoretical predictions agree well with the experimental observations. The difference between these curves is only due to the effect of induced capillary dipoles which grow with the size of the particles. The fits of the asymmetric 800-400 pair and 800-500 pair, the green and turquoise curves respectively, are obtained using Δz as the only fitting parameter. Due to geometrical considerations, Δz is constrained between $0\,\mu m$ and $330\,\mu m$, the height between the center of the $800\,\mu m$ bead and its contact line. We obtain $\Delta z = 270\,\mu m$ for the 800-400 pair and $\Delta z = 300\,\mu m$ for the 800-500 pair. For a distance above $1000\,\mu m$ between the two beads, the magnetic repulsion reduction factor $[1 - 3(\Delta z/\lambda x_{ij})^2] \gtrsim 0.7$. Since the magnetic reduction has a weak effect, the deviations from the model in Fig. 3 were therefore mostly due to induced capillary dipoles and nonlinear terms in Eq. (10). For asymmetrical cases, it should be remarked that the fits using Eq. (10) capture very well the threshold below which beads come into contact. This gives us the precise magnitude of the magnetic field B_z at which capillary attraction overcomes magnetic repulsion, leading to contact
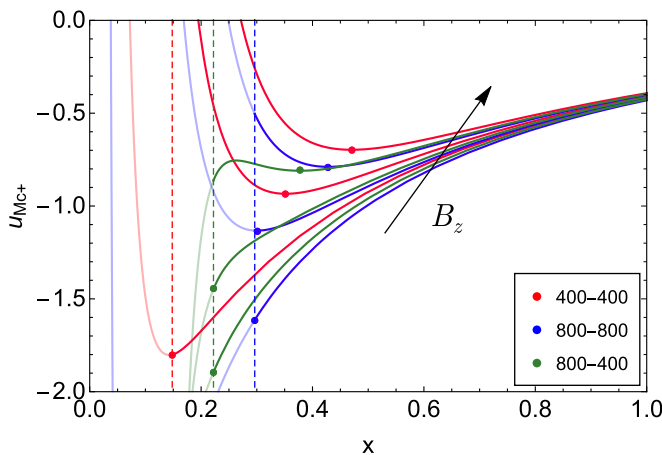
FIG. 4. Dimensionless magnetocapillary interaction potential $u_{\mathrm{Mc+}}$ as a function of normalized interdistance $x = r/\lambda$ for three different B_z values increasing as the black arrow. Dots indicate the minimum of each potential corresponding to the equilibrium distance reported in Fig. 3(a). Vertical dashed lines are contact bead situations.

between the beads. We can conclude that all data are wellfitted by the induced capillary dipole model.

Figure 4 presents the dimensionless interaction potential $u_{\mathrm{Mc+}}$ as a function of normalized distance x for the three pairs studied in Fig. 3(a) and for three different vertical magnetic field values $B_z = \{7, 23, 34\}$ G. These values correspond to the magnetic field at which each pair of beads come into contact. The minimum of each potential is given by the colored dots indicating the dimensionless equilibrium distance $x^\star$ between the two particles. For the symmetrical situations (blue and red curves), one observes that larger objects, i.e., larger dipolar moments aQ, imply shorter equilibrium distances. This difference between equilibrium distances is significant at short distances, i.e., for low B_z values. For asymmetrical cases, the situation is more pronounced. A new feature also appears: a second minimum may develop at contact due to some attractive magnetic interaction instead of short-range repulsion. For a range of B_z values, contacting beads and separated beads may coexist at equilibrium. On top of that, the potential $u_{\mathrm{Mc+}}$ for asymmetric cases (in green) is much lower than for symmetric cases, which means that asymmetric cases are more cohesive situations. This is due to the induced capillary dipoles, which are enhanced in asymmetric cases. An assembly of beads of different sizes could take advantage of these bonds and be more functionalized [40].

Moreover, our nice experiment allows us to estimate the lateral capillary force F_c between particles directly by measuring the magnetic force counterbalancing it at equilibrium. This method has also been used to measure the capillary forces between floating magnetic colloids under magnetic field by Helseth and Fischer [41]. Experimental measurements of the dimensionless capillary force for all pairs of particles are presented in Fig. 5. When the beads are far from each other, the contact lines are horizontal, $U_{Qd} = 0$, such that the capillary force is only given by $F_c = -\partial(U_{QQ})/\partial r$. For the symmetrical pairs 400-400, 500-500, and 800-800, we can therefore define a subset of the data with large values of $r^\star$, where the measurement of the force directly provides access to the capillary charges by their product. We obtain capillary charges of $-5\,\mu\mathrm{m}$, $-11\,\mu\mathrm{m}$, and $-42\,\mu\mathrm{m}$ for the $400\,\mu\mathrm{m}$, $500\,\mu\mathrm{m}$, and $800\,\mu\mathrm{m}$ beads, respectively, which aligns with the expected values from Eq. (2) with a contact angle $\theta \approx 75°$. The colored curves in Fig. 5 represent the dimensionless capillary forces predicted by our model $F_c = -\partial(U_{QQ} + U_{Qd})/\partial r$, while the black curve does not consider the tilt of the contact line. Once again, we observe a good agreement between the experimental data and our induced capillary dipoles model.
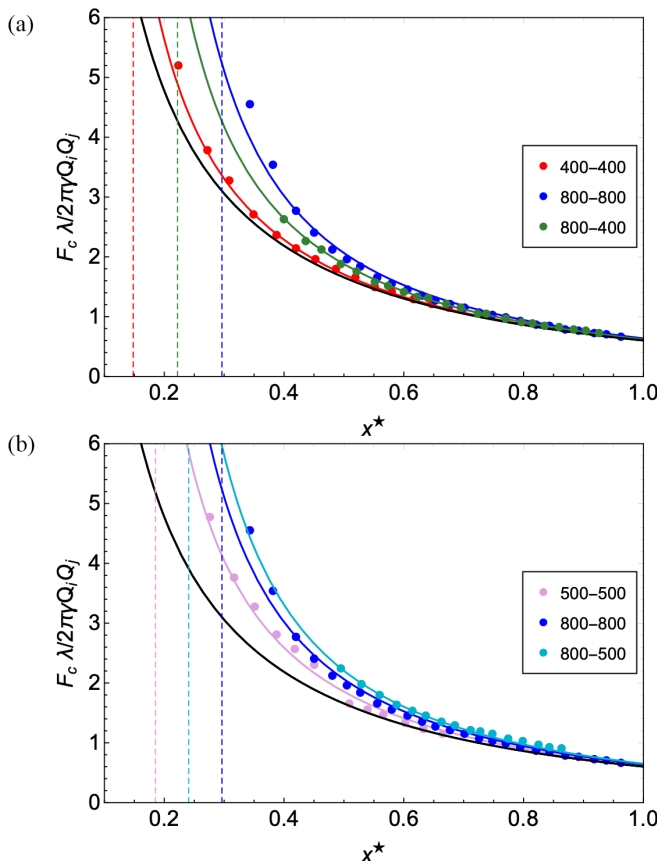
FIG. 5. Experimental data of the dimensionless capillary force as a function of the normalized interdistance r/λ for (a): pairs of $d = 400$ μm and $d = 800$ μm, and the asymmetrical case $d_1 = 400$ μm and $d_2 = 800$ μm and (b): pairs of $d = 500$ μm and $d = 800$ μm, and the asymmetrical case $d_1 = 500$ μm and $d_2 = 800$ μm. Colored curves are capillary forces derived from the potential $U_{QQ} + U_{Qd}$. The black curve is the capillary force derived from the potential U_{QQ} from Eq. (3) only. Vertical dashed lines are contact bead situations.

At $r^\star/\lambda = 0.45$, we observe an extra attraction of 4% for the 400-400 pair, 19% for the 500-500 pair, and 30% for the 800-800 pair. For these identical pairs, such increases are consistent with the numerical observations of Cooray *et al.* [29]. The asymmetrical 800-400 pair exhibits 16% of extra attraction which is less than the 800-800 pair. However, when the 400 μm bead is replaced with a 500 μm bead, forming an 800-500 pair, an additional attraction of 41% is observed. Interestingly, in the case of the asymmetrical pair 800-500, we observe a further increase in attraction compared to the 800-800 pair, despite a smaller product of charges in the U_{QQ} potential. This behavior can be explained by induced dipoles and the resulting nonlinearity of the model described in Eq. (10).

The next relevant question is: can we visualize the effects of capillary dipoles on floating particle assemblies? The answer is affirmative. Figure 6 shows various pictures of self-assemblies. The first picture (a) shows an assembly of $N = 9$ equivalent beads (diameter 400 μm) which is compared to (b), a similar assembly in which a small bead is replaced by a much larger one (diameter 800 μm). The monodisperse assembly is a tiny floating crystal with sixfold symmetry as expected from an isotropic interaction. Please remark that fivefold defects could be observed on larger assemblies but it relies on local curvature effects [19]. However, when a large bead is present, one first observes that other beads are surrounding this bead in order to favor as much as possible asymmetrical binding, which has lower potential energy as shown in Fig. 4. Here the large central bead can have up to eight
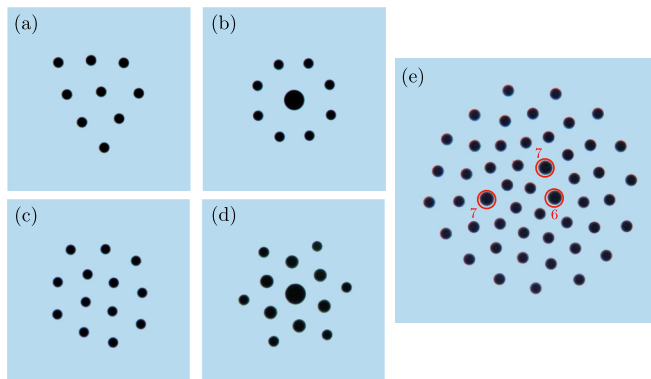
FIG. 6. Various typical pictures of magnetocapillary self-assemblies. (a) Floating crystal of $N = 9$ small beads (400 µm in diameter). (b) Similar system having one bead being replaced by a large one (800 µm in diameter): the crystal now has an octagonal symmetry. (c) Floating crystal of $N = 13$ beads. (d) Seven small beads are replaced by one large and six medium ones leading to a perfect flowerlike self-assembly having a nice crystal ordering (sixfold symmetry). (e) Large binary self-assembly of 400 µm and 500 µm floating particles. The 500 µm beads (in red) have six or seven neighbors.

neighbors. From what we discussed above, this octagonal symmetry is quite surprising because the asymmetrical binding is shorter than symmetrical bonds. In fact, the central bead is not polarized because all dipoles are canceling. However, strong induced dipoles on peripheral beads are all pointing to the central bead. One understands that in that case, the neighboring dipoles are forming angles around 45°, a configuration that provides a strong extra attraction in between peripheral beads allowing for eight beads to surround the heavy central one. A similar situation is shown in Figs. 6(c) and (d) for the $N = 13$ beads system. For that specific number, identical beads are always forming a tiny floating assembly with few symmetrical features: a rhombus of four beads surrounded by nine beads. However, by changing a small bead with a large one (800 µm) and six small beads with medium ones (500 µm), a flower is formed. Again, large beads tend to be surrounded by a shell of medium ones, themselves surrounded by small ones. This trick can be used to form a perfect floating crystal at liquid interfaces. In much larger floating crystals of identical particles, the induced dipoles in various directions may cancel. In that case, sixfold symmetry is expected and some fivefold defects may appear depending on the curvature of the interface [19]. No sevenfold defect has ever been observed for identical particles. When some particles are replaced by larger ones, as shown in Fig. 6(e), one observes sevenfold defects induced by the larger particles. Binary floating systems may therefore reach a higher degree of complexity. This is left for future works.

In summary, an extra attraction is observed between close floating objects due to the tilt of their contact lines. In the capillary charge approach, this effect can be captured by considering the apparition of induced capillary dipoles. This model is found to fit our experimental data accurately. Moreover, we found that asymmetrical situations are enhancing this phenomenon, and we discussed these effects in regard to real self-assemblies. Since capillary-driven self-assembly is encountered in many applications, our findings contribute to reaching much higher degrees of complexity. Exploiting such effects could be of high interest to create specific structures that can be functionalized, for example, to obtain locomotion [42].

[1] B. A. Grzybowski, H. A. Stone, and G. M. Whitesides, Dynamic self-assembly of magnetized, millimetre-sized objects rotating at a liquid-air interface, Nature (London) **405**, 1033 (2000).

[2] G. M. Whitesides and B. Grzybowski, Self-assembly at all scales, Science **295**, 2418 (2002).

[3] J. A. Pelesko, *Self assembly: the science of things that put themselves together* (Chapman and Hall/CRC, 2007).

[4] P. A. Kralchevsky and K. Nagayama, Capillary forces between colloidal particles, Langmuir **10**, 23 (1994).

[5] K. D. Danov and P. A. Kralchevsky, Capillary forces between particles at a liquid interface: General theoretical approach and interactions between capillary multipoles, Adv. Colloid Interface Sci. **154**, 91 (2010).

[6] M. Poty, G. Lumay, and N. Vandewalle, Customizing mesoscale self-assembly with three-dimensional printing, New J. Phys. **16**, 023013 (2014).

[7] N. Bowden, A. Terfort, J. Carbeck, and G. M. Whitesides, Self-assembly of mesoscale objects into ordered two-dimensional arrays, Science **276**, 233 (1997).

[8] M. Vilfan, A. Potočnik, B. Kavčič, N. Osterman, I. Poberaj, A. Vilfan, and D. Babič, Self-assembled artificial cilia, Proc. Natl. Acad. Sci. USA **107**, 1844 (2010).

[9] A. Rida and M. Gijs, Manipulation of self-assembled structures of magnetic beads for microfluidic mixing and assaying, Anal. Chem. **76**, 6239 (2004).

[10] S. E. Chung, W. Park, S. Shin, S. A. Lee, and S. Kwon, Guided and fluidic self-assembly of microstructures using railed microfluidic channels, Nat. Mater. **7**, 581 (2008).

[11] M. Boncheva and G. M. Whitesides, Making things by self-assembly, MRS Bull. **30**, 736 (2005).

[12] L. Zhang, J. M. Chan, F. X. Gu, J.-W. Rhee, A. Z. Wang, A. F. Radovic-Moreno, F. Alexis, R. Langer, and O. C. Farokhzad, Self-assembled lipid- polymer hybrid nanoparticles: a robust drug delivery platform, ACS Nano **2**, 1696 (2008).

[13] F. Martinez-Pedrero and P. Tierno, Magnetic Propulsion of Self-Assembled Colloidal Carpets: Efficient Cargo Transport via a Conveyor-Belt Effect, Phys. Rev. Appl. **3**, 051003(R) (2015).

[14] J. B. Edel, A. A. Kornyshev, and M. Urbakh, Self-assembly of nanoparticle arrays for use as mirrors, sensors, and antennas, ACS Nano **7**, 9526 (2013).

[15] S.-H. Kim, S. Y. Lee, S.-M. Yang, and G.-R. Yi, Self-assembled colloidal structures for photonics, NPG Asia Materials **3**, 25 (2011).

[16] Y. Xia, B. Gates, and Z.-Y. Li, Self-assembly approaches to three-dimensional photonic crystals, Adv. Mater. **13**, 409 (2001).

[17] I. Ho, G. Pucci, and D. M. Harris, Direct Measurement of Capillary Attraction between Floating Disks, Phys. Rev. Lett. **123**, 254502 (2019).

[18] M. Poty and N. Vandewalle, Equilibrium distances for the capillary interaction between floating objects, Soft Matter **17**, 6718 (2021).

[19] N. Vandewalle, L. Clermont, D. Terwagne, S. Dorbolo, E. Mersch, and G. Lumay, Symmetry breaking in a few-body system with magnetocapillary interactions, Phys. Rev. E **85**, 041402 (2012).

[20] G. Grosjean, G. Lagubeau, A. Darras, M. Hubert, G. Lumay, and N. Vandewalle, Remote control of self-assembled microswimmers, Sci. Rep. **5**, 16035 (2015).

[21] D. Vella and L. Mahadevan, The "Cheerios effect", Am. J. Phys. **73**, 817 (2005).

[22] D. Chan, J. Henry Jr, and L. White, The interaction of colloidal particles collected at fluid interfaces, J. Colloid Interface Sci. **79**, 410 (1981).

[23] P. A. Kralchevsky and N. D. Denkov, Capillary forces and structuring in layers of colloid particles, Curr. Opin. Colloid Interface Sci. **6**, 383 (2001).

[24] P. A. Kralchevsky and K. Nagayama, Capillary interactions between particles bound to interfaces, liquid films and biomembranes, Adv. Colloid Interface Sci. **85**, 145 (2000).

[25] M.-J. Dalbe, D. Cosic, M. Berhanu, and A. Kudrolli, Aggregation of frictional particles due to capillary attraction, Phys. Rev. E **83**, 051403 (2011).

[26] M. M. Nicolson, The interaction between floating particles, Math. Proc. Cambridge Philos. Soc. **45**, 288 (1949).

[27] D. Vella, Floating versus sinking, Annu. Rev. Fluid Mech. **47**, 115 (2015).

[28] D. Stamou, C. Duschl, and D. Johannsmann, Long-range attraction between colloidal spheres at the air-water interface: The consequence of an irregular meniscus, Phys. Rev. E **62**, 5263 (2000).

[29] H. Cooray, P. Cicuta, and D. Vella, Floating and sinking of a pair of spheres at a liquid–fluid interface, Langmuir **33**, 1427 (2017).

[30] C. Raufaste, G. Kirstetter, F. Celestini, and S. Cox, Deformation of a free interface pierced by a tilted cylinder, Europhys. Lett. **99**, 24001 (2012).

[31] H. Cooray, P. Cicuta, and D. Vella, The capillary interaction between two vertical cylinders, J. Phys.: Condens. Matter **24**, 284104 (2012).

[32] G. B. Davies and L. Botto, Dipolar capillary interactions between tilted ellipsoidal particles adsorbed at fluid–fluid interfaces, Soft Matter **11**, 7969 (2015).

[33] B. J. Newton, R. Mohammed, G. B. Davies, L. Botto, and D. M. A. Buzza, Capillary interaction and self-assembly of tilted magnetic ellipsoidal particles at liquid interfaces, ACS Omega **3**, 14962 (2018).

[34] N. Bowden, I. S. Choi, B. A. Grzybowski, and G. M. Whitesides, Mesoscale self-assembly of hexagonal plates using lateral capillary forces: Synthesis using the "capillary bond," J. Am. Chem. Soc. **121**, 5373 (1999).

[35] G. Lagubeau, G. Grosjean, A. Darras, G. Lumay, M. Hubert, and N. Vandewalle, Statics and dynamics of magnetocapillary bonds, Phys. Rev. E **93**, 053117 (2016).

[36] R. Chinomona, J. Lajeunesse, W. H. Mitchell, Y. Yao, and S. E. Spagnolie, Stability and dynamics of magnetocapillary interactions, Soft Matter **11**, 1828 (2015).

[37] G. Grosjean, M. Hubert, G. Lagubeau, and N. Vandewalle, Realization of the najafi-golestanian microswimmer, Phys. Rev. E **94**, 021101(R) (2016).

[38] G. Grosjean, M. Hubert, and N. Vandewalle, Magnetocapillary self-assemblies: Locomotion and micro-manipulation along a liquid interface, Adv. Colloid Interface Sci. **255**, 84 (2018).

[39] Y. Collard, F. N. Piñan Basualdo, A. Bolopion, M. Gauthier, P. Lambert, and N. Vandewalle, Controlled transitions between metastable states of 2d magnetocapillary crystals, Sci. Rep. **12**, 16027 (2022).

[40] M. Hubert, O. Trosman, Y. Collard, A. Sukhov, J. Harting, N. Vandewalle, and A.-S. Smith, Scallop Theorem and Swimming at the Mesoscale, Phys. Rev. Lett. **126**, 224501 (2021).

[41] L. E. Helseth and T. M. Fischer, Particle interactions near the contact line in liquid drops, Phys. Rev. E **68**, 042601 (2003).

[42] Y. Collard, G. Grosjean, and N. Vandewalle, Magnetically powered metachronal waves induce locomotion in self-assemblies, Commun. Phys. **3**, 112 (2020).